Journal of Materials Chemistry A

RSC Publishing

PAPER

View Article Online
View Journal | View Issue

Cite this: J. Mater. Chem. A, 2013, 1, 14633

Structure, properties and formation of $PuCrO_3$ and $PuAlO_3$ of relevance to doped nuclear fuels

Michele L. Fullarton,[a] Meng J. Qin,[a] Marc Robinson,[b] Nigel A. Marks,[b] Daniel J. M. King,[ac] Eugenia Y. Kuo,[a] Gregory R. Lumpkin[a] and Simon C. Middleburgh*[a]

Received 18th July 2013
Accepted 5th October 2013

DOI: 10.1039/c3ta12782f

www.rsc.org/MaterialsA

We have employed a variety of computational methods to understand the behaviour of Pu, generated by neutron capture reactions in UO_2 fuel, with Cr_2O_3 and Al_2O_3, two common UO_2 fuel dopants. Structure search calculations using density functional theory and empirical potentials show that $PuCrO_3$ and $PuAlO_3$ are likely to form in these systems. The lowest energy structure adopted by both compounds is predicted to be the orthorhombic (*Pnma*) $GdFeO_3$-type perovskite structure. Relative to UO_2, the thermal conductivity of $PuCrO_3$ was calculated to be approximately three times smaller over the explored temperature range and therefore the presence of this phase will impact the microstructure, fission product distribution and gas release properties of UO_2-based fuels. In contrast, the $PuAlO_3$ phase had a similar thermal conductivity to UO_2. Calculated defect energies suggest that defects in both $PuCrO_3$ and $PuAlO_3$ will be dominated by antisite defects and that their radiation tolerances are similar to that of UO_2. Calculation of the solution and partition energies of a range of trivalent cations indicate that minor actinides are likely to substitute for Pu in the perovskite structure having an impact on the in-reactor behaviour of Cr-containing fuels and subsequently the waste reprocessing route.

1 Introduction

Recently, there has been considerable research into increasing the efficiency and safety of nuclear fuels, with particular focus on UO_2, but increasingly on MOX fuels (blended PuO_2, UO_2 and occasionally other actinide oxides such as ThO_2 (ref. 1) and Am_2O_3 (ref. 2)). By increasing the burn-up it is possible to extract more power from a fuel which in turn can improve the economic efficiency. However, the harsher environments (larger radiation doses and often higher temperatures) induced by a higher burn-up pose new challenges in predicting the behaviour of the fuel and the methods in which it can be safely used and disposed of.[3] In addition, by understanding the segregation and behaviour of fission products in fuels (including doped fuels[4]), the separation of long-lived isotopes can be carried out more efficiently at a lower cost to the utility and ultimately the consumer.

One particular complication resulting from an increase in burn-up is the development of high burn-up structure (HBS) and an increase in minor actinides and Pu in the pellet rim region. The HBS formation is thought to be primarily due to radiation damage[5] but may also be a consequence of an increase in the concentration of fission products.[6,7] This restructuring affects the outer radius of the fuel, or rim, which operates at a lower temperature than the centre line of the fuel pellet and may have knock-on effects on processes occurring deeper within the fuel.[5]

Various dopants can be added to improve the in-reactor behaviour of fuels.[8,9] Additives such as Cr_2O_3 (occasionally with Al_2O_3 (ref. 4)) or SiO_2 change the fuel microstructure; in the case of Cr_2O_3, inclusion increases grain size and density. With an increase in grain size, the release of fission gasses is expected to decrease, due to both the suppression of intergranular porosity and the extension of gas atom migration pathways to grain boundaries.[4,9]

In addition to the alterations to the micro-structure mentioned above, dopants are expected to interact with the fission products that form in-reactor. Previous work by Cooper *et al.*[10] has shown the stability of Al–Cr–U–O phases in oxidising conditions (*i.e.* UO_{2+x}), but explain that they are not stable in reducing atmospheres. Around the rim of the pellet, preferential oxidation of the Zr cladding material results in a stoichiometric (or hypo-stoichiometric) fuel.[11] Furthermore, the cladding shielding effect results in ^{238}U undergoing neutron capture and subsequent beta decay,[12] producing a high concentration of Pu and further minor actinides upon neutron capture. Due to the reducing environment of the rim structure, the Pu and minor actinides are expected to exist as trivalent cations.[13]

Precipitates that may form as a result of additive-fission product interaction, (*e.g.* $PuCrO_3$ or $PuAlO_3$) may have significant

[a]IME, Australian Nuclear Science and Technology Organisation, New Illawarra Road, Lucas Heights, NSW, Australia. E-mail: simm@ansto.gov.au

[b]Nanochemistry Research Institute, Curtin University, Perth, Western Australia, Australia

[c]Institute for Nanoscale Technology, University of Technology, Sydney, NSW, Australia

benefits as minor actinide getters, acting as a host for easy immobilisation and then, potentially, for conversion to isotopes with shorter half-lives. Understanding the accommodation processes and stability of the compounds will guide design for a waste form which has a greater resistance to leaching and aptitude for geological disposal.[14] The precipitates may also function as an absorber of volatile fission products, capturing elements such as Cs and I within the structure and preventing them from entering the free volume and interacting with the cladding, although this is not considered in this body of work.

Previous work has confirmed the formation of $PuCrO_3$ and $PuAlO_3$ (ref. 15) and Levy[16] used simulations based on empirical inter-atomic potentials to study the compounds. Russell *et al.*[15] investigated a range of $PuXO_3$ systems (with Pu in both 3+ and 4+ charge states) with X-ray diffraction methods and reported the experimental crystal structures and lattice constants for each compound. They reported that $PuCrO_3$ has an orthorhombic crystal structure with lattice constants 5.46 Å, 5.51 Å and 7.76 Å, and that $PuAlO_3$ has a rhombohedral crystal structure with a lattice constant of 5.33 Å and with $\alpha \equiv \beta \equiv \gamma = 56^\circ 4'$. They did find however, that $PuAlO_3$ exhibited a degree of structural variation with changes in temperature, but neither the extent of the variance nor the structure evolution were made clear.

To improve understanding of the behaviour of $PuCrO_3$ and $PuAlO_3$ in fuel, we have verified their structures by computer simulations, using both an empirical description of atomic bonding and an *ab initio* approach. In addition, we have studied their defect behaviour, predicted the drive for cation partition into the secondary phase and predicted the effects of the secondary phase formation on the thermal behaviour of the doped fuel. Combined with previous work on Cr-containing secondary phases,[10,17–19] a complete understanding of the effect of Cr doping on UO_2 fuels is emerging.

2 Approach and methodology

For each oxide under investigation, four types of calculations were carried out: structure optimisations, defect energy calculations, solution/partition energy calculations and the determination of thermal conductivities.

To verify the structures of both $PuCrO_3$ and $PuAlO_3$, a number of analogue crystal structures were simulated and their stabilities (with Cr/Al and Pu occupying the cation sites) compared with each other. The evolutionary structure prediction code USPEX[20] was also used to predict the most stable $PuCrO_3$ and $PuAlO_3$ structure.

Six possible $A^{3+}B^{3+}O_3{}^{2-}$ analogues were identified and modified to simulate $PuCrO_3$ and $PuAlO_3$. These were the $LiNbO_3$ ($R3c$)-type structure, $GdFeO_3$ ($Pnma$)-type structure, $SrTiO_3$ ($Pm\bar{3}m$)-type structure, $NdAlO_3$ ($R\bar{3}c$)-type structure, $LaAlO_3$ ($R\bar{3}m$) and the $BiMnO_3$ ($C2/c$)-type structure. These structures are all related to the $SrTiO_3$ perovskite structure, either showing distortions or displacements over one or both the anion or cation sublattices. The structures chosen make up a fraction of the possible perovskite-related structures, but encompass the various families of structures, thus allowing the lowest energy structure to be identified.

Full geometry optimisations were carried out under constant pressure on each structure analogue (with no symmetry constraints) using both the empirical GULP[21] program and the *ab initio*, density functional theory (DFT) code, VASP.[22] Each of these codes calculates a lattice energy that allows the stabilities of the lattice structures to be compared and the reaction enthalpies to be predicted.

The short-range interactions in GULP were described using the parametrised Buckingham potential[23] (previously published[18,24,25]) while the long-range interactions were considered to be dominated by Coulombic interactions. Each of the ions was treated as fully charged (*i.e.* oxygen has an overall 2^- charge). A core–shell interaction was applied to the oxygen ion to account for the polarisability of the ion.[26]

VASP calculations used the projector augmented wave (PAW) pseudopotentials with the GGA-PBE exchange correlation.[27] A Mott–Hubbard correction was applied to the Pu ion ($U = 4.00$ eV and $J = 0.70$ eV as used by ref. 28). Unique k-point grids with similar spacing (0.07 Å^{-1}) for each structure were used with a cut-off energy of 400 eV, giving an accuracy of over 10^{-3} eV per unit cell.

USPEX, a crystal structure prediction code,[20] was used with GULP to compare its predictions with the lowest energy structures predicted by VASP and GULP. USPEX was allowed to search through all 230 possible space groups using 4 atoms of Cr, 4 of Pu and 12 of O in the primitive unit cell. At each generation, twenty structures were generated and their lattice energies calculated (using GULP) and compared. The structures in subsequent generations were produced as follows: 50% of the structures were constructed from the lowest energy structures of the previous generation, 10% from random space groups, 20% from permutations and 20% from mutation of the lattice. This process continued until the lattice energy remained the same for 20 generations in a row.

Once confident that the lowest energy structure had been identified, the defect energies, solution energies and partition energies were calculated using GULP. A Mott–Littleton approach[29] was used whereby concentric spherical regions were centred within ± 0.001 fractional coordinate of the point defect (both intrinsic and extrinsic defects were considered). Region I had a radius of 10 Å, region IIa a radius of 30 Å (giving an accuracy greater than 0.005 eV per defect) and region IIb extended to infinity. The results were used to make predictions about the defect behaviour of the compounds.

Thermal conductivities were calculated using the non-equilibrium molecular dynamics approach of Müller-Plathe[30] as implemented in the Large-scale Atomic/Molecular Massively Parallel Simulator (LAMMPS).[31] A heat flux was imposed along the a-axis of UO_2 (with a cross section of 32.81×32.81 Å), and along both the a-axis and c-axis of both $PuCrO_3$/$PuAlO_3$ supercells (with a cross section of 27.42×27.75 Å/26.82×26.87 Å). The average temperature gradient was measured after a state of linear response was established – typically this was around 100 ps. Values of thermal conductivity were calculated for a range of lengths. Bulk values were then determined through extrapolation to infinite length (and averaged along each principle axis when non-cubic). All simulations were calculated with periodic boundary conditions and a time-step of 1 fs.

Table 1 Calculated lattice energies, lattice binding energies and reaction enthalpies (from reaction (1)) for simulated $PuCrO_3$

Structures for $PuCrO_3$ stability calculations	VASP		GULP	
	Binding energy (eV)	ΔH_f (eV)	Lattice energy (eV)	ΔH_f (eV)
Pu_2O_3	−55.95	—	−128.18	—
Cr_2O_3	−43.47	—	−152.54	—
$GdFeO_3$ (orthorhombic)	−50.27	−0.56	−140.57	−0.20
$BiMnO_3$ (monoclinic)	−50.14	−0.43	−140.50	−0.14
$LiNbO_3$ (hexagonal)	−50.14	−0.42	−140.50	−0.14
$LaAlO_3$ (rhombohedral)	−49.56	0.15	−140.11	0.25
$NdAlO_3$ (hexagonal)	−49.49	0.22	−140.50	−0.14
$CaTiO_3$ (cubic)	−48.96	0.75	−140.11	0.25

Table 2 Calculated lattice energies, lattice binding energies and reaction enthalpies for simulated $PuAlO_3$

Structures for $PuAlO_3$ stability calculations	VASP		GULP	
	Binding energy (eV)	ΔH_f (eV)	Lattice energy (eV)	ΔH_f (eV)
Pu_2O_3	−55.95	—	−128.18	—
Al_2O_3	−37.46	—	−159.65	—
$GdFeO_3$ (orthorhombic)	−47.11	−0.41	−143.99	−0.08
$BiMnO_3$ (monoclinic)	−47.09	−0.38	−143.99	−0.07
$LiNbO_3$ (hexagonal)	−47.05	−0.34	−143.98	−0.07
$LaAlO_3$ (rhombohedral)	−47.02	−0.31	−143.94	−0.03
$NdAlO_3$ (hexagonal)	−47.00	−0.30	−143.94	−0.02
$CaTiO_3$ (cubic)	−47.01	−0.30	−143.94	−0.02

3 Results

3.1 $PuCrO_3$ and $PuAlO_3$ structure prediction

Reaction enthalpies for $PuCrO_3$ in the six perovskite structure types listed in Section 2 were computed using DFT and empirical potentials. The enthalpy was computed using eqn (1):

$$\frac{1}{2}Cr_2O_3 + \frac{1}{2}Pu_2O_3 \rightarrow PuCrO_3 \quad (1)$$

where Cr_2O_3 and Pu_2O_3 are in their standard states, namely corundum and hexagonal La_2O_3-type, respectively. The total energies as computed by VASP and GULP, and the associated reaction enthalpies, are reported in Table 1. The calculated energies for the six perovskite structures are listed in the table in order of decreasing stability as determined by VASP. The most stable structure is the orthorhombic $GdFeO_3$-type phase shown in Fig. 1. GULP calculations also found this structure to be the most stable, and across the six structures there is broad agreement with VASP (although the energies should not be directly compared due to the differing methods).

Of the six structure analogues, both approaches resulted in negative reaction enthalpies for the $LiNbO_3$-type, $GdFeO_3$-type and $BiMnO_3$-type structures, indicating they are stable. Of these three structures, the $GdFeO_3$-type structure (see Fig. 1) was found to have the lowest formation enthalpy by both empirical and DFT methods, −0.20 eV and −0.56 eV respectively. This was supported by USPEX calculations which indicated the *Pmna* orthorhombic structure was the most stable.

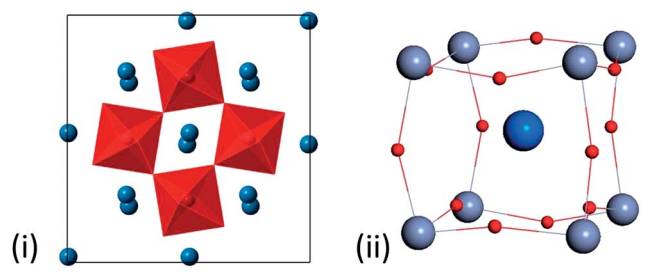

Fig. 1 The predicted lowest energy structure of $PuCrO_3$ – the *Pmna* orthorhombic structure – (i) illustrates the structure viewed down the *z*-axis, highlighting the Cr–O octahedral distortions (red polyhedra) around the Pu ions (blue). (ii) Illustrates the perovskite single unit cell with oxygen distortion around the Cr ions (grey).

The optimization of $PuCrO_3$, with the *Pmna* orthorhombic structure, resulted in lattice parameters of: $a = 5.485$ Å, $b = 5.551$ Å, and $c = 7.796$ Å, when calculated using GULP and $a = 5.443$ Å, $b = 5.512$ Å, and $c = 7.686$ Å, when calculated using VASP. This compares to 5.46 Å, 5.59 Å and 7.76 Å reported by Russell *et al.*[15] – which is in good agreement with both simulation methods. In the lowest energy structure, the Cr^{3+} ions take up the 4b site $\left(0, \frac{1}{2}, \frac{1}{2}\right)$, the Pu^{3+} ions take up the 4c $\left(-0.0153, 0.063, \frac{1}{4}\right)$ site, the four O_I^{2-} take up a different 4c $\left(0.100, 0.468, \frac{1}{4}\right)$ site and the eight O_{II}^{2-} occupy the 8d (0.697, 0.301, 0.053) site.

The structure of $PuAlO_3$ was investigated in a similar manner to that for $PuCrO_3$. The resultant lattice energies and reaction enthalpies are reported in Table 2.

In contrast to $PuCrO_3$, reaction enthalpies for all six structures were found to be negative with minimal quantitative differences. The most stable structure with the lowest reaction enthalpy was again found to be the $GdFeO_3$-type structure by both GULP and VASP. Optimisation of cell dimensions resulted in: $a = 5.364$ Å, $b = 5.373$ Å and $c = 7.591$ Å when calculated in GULP, and $a = 5.353$ Å, $b = 5.344$ Å, and $c = 7.536$ Å, when calculated using VASP. The lattice constants have all decreased in comparison to those for $PuCrO_3$. The reduction in lattice parameters relative to $PuCrO_3$ can be attributed to the smaller ionic radius of Al^{3+} (0.535 Å) when compared to Cr^{3+} (0.615 Å).[32] This result is at odds with the room temperature structure prediction by Russell *et al.*[15] who predicted a rhombohedral perovskite phase. A high temperature (including room temperature) phase change could be the reason for the clear discrepancy. In the following section we consider both the orthorhombic structure and the rhombohedral structure of $PuAlO_3$ when predicting the thermal conductivity of the compound.

3.2 Thermal conductivity of $PuCrO_3$ and $PuAlO_3$

Non-equilibrium molecular dynamics simulations were carried out to determine the effect the formation of the $PuCrO_3$ defect perovskite structure has on the thermal conductivity of Cr/Al doped UO_2 fuel. The potentials described in Section 2 were used to calculate the thermal

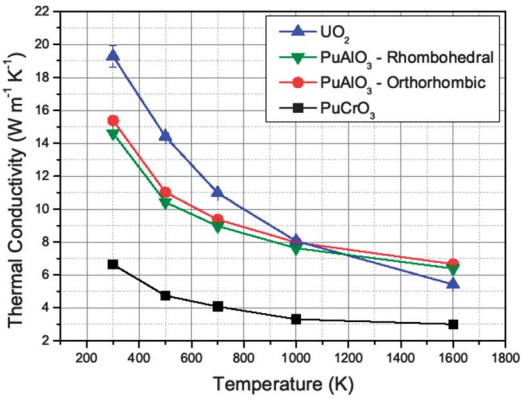

Fig. 2 Variation of thermal conductivity with temperature of stoichiometric UO_2, $PuCrO_3$ and $PuAlO_3$ (both rhombohedral and orthorhombic lattices).

conductivities of stoichiometric UO_2, $PuCrO_3$ and $PuAlO_3$ at temperatures ranging from 300 to 1600 K, as shown in Fig. 2. The thermal conductivity of the orthorhombic structures are averaged over their principle axes.

The thermal conductivity of UO_2 was found to be ~3 times greater than that of $PuCrO_3$ within the temperature range. The predicted thermal conductivity of UO_2 is in good agreement with the un-corrected values of Watanabe *et al.*[40] who used the same potential set as the one used in this work. They corrected their results, adding the results of anharmonic effects in UO_2, by using experimental values of the thermal conductivity and bulk modulus – values we do not have for both the $PuCrO_3$ and $PuAlO_3$ compounds. As such, the values presented should be treated in a qualitative manner (owing to the consistent potential set being used for all of the compounds).

The decrease in thermal conductivity of the material due to the presence of $PuCrO_3$ has implications for the thermal behaviour of Cr-doped fuels and will therefore have knock-on effects on the gas release properties, structure and fission product accommodation. Examples in literature show marked structural differences between standard fuel pellets and doped pellets after irradiation. Arborelius *et al.*[4] provide a comparison between a doped fuel and a standard UO_2 pellet. The doped pellet developed a centre-line hole surrounded by columnar grains indicating restructuring, possibly due to an increase in the centre-line temperature of the pellet caused by the poorer thermal conductivity of the pellet as a result of Cr forming precipitates.

Both $PuAlO_3$ structures (the predicted low energy orthorhombic and the experimentally observed rhomobohedral systems) were predicted to have a higher thermal conductivity than the $PuCrO_3$ system. At higher temperatures the thermal conductivity is greater than that of stoichiometric UO_2 meaning that the thermal impact that this oxide has on the fuel is lower. As the structure of the two orthorhombic perovskite structures are the same, the difference in thermal conductivity is likely solely related to the variation in bonding between the B cation and the oxygen (stiffer in $PuAlO_3$ compared to $PuCrO_3$) although density may also play a minor role.

Table 3 $PuCrO_3$ defect energies calculated using the Mott–Littleton method

Defect	Defect energy (eV)			
Vacancies				
Pu vacancy	44.09			
Cr vacancy	57.02			
O_I vacancy	19.98			
O_{II} vacancy	19.89			
Interstitials				
Site	$\left(\frac{1}{8},\frac{7}{9},\frac{1}{8}\right)$	$\left(\frac{3}{40},\frac{37}{40},0\right)$	$\left(\frac{2}{3},\frac{3}{20},\frac{1}{4}\right)$	$\left(\frac{3}{10},\frac{9}{20},\frac{2}{25}\right)$
Pu interstitial	−23.56	−23.56	−24.24	−23.54
Cr interstitial	−40.34	−39.31	−40.38	−40.08
O interstitial	−9.07	−9.43	−10.16	−10.10
Anti-sites				
Pu on Cr site	14.08			
Cr on Pu site	−9.78			

3.3 Defect behaviour and radiation tolerance of $PuCrO_3$ and $PuAlO_3$

The type and population of defects under both equilibrium and non-equilibrium conditions provides insight into the stability and behaviour of a material. Elastic collisions of fission products with the ions in the lattice are the primary cause of radiation damage in a structure.[33] The collisions produce Frenkel pairs (see eqn (2)–(4)), Schottky (eqn (5)) and anti-site defects (eqn (6)). Kröger–Vink notation is used to describe the defects.[37] The greater the ability of the lattice to accommodate these defects, the greater its radiation tolerance will be.[33,34] To make predictions about the radiation tolerance of $PuCrO_3$, the vacancy, interstitial and anti-site defect energies were calculated for the lowest energy *Pnma* structure using GULP. These are reported in Table 3.

$$Pu_{Pu}^{\times} \rightarrow Pu_i^{\bullet\bullet\bullet} + V_{Pu}^{\prime\prime\prime} \quad (2)$$

$$Cr_{Cr}^{\times} \rightarrow Cr_i^{\bullet\bullet\bullet} + V_{Cr}^{\prime\prime\prime} \quad (3)$$

$$O_O^{\times} \rightarrow O_i^{\prime\prime} + V_O^{\bullet\bullet} \quad (4)$$

$$Pu_{Pu}^{\times} + Cr_{Cr}^{\times} + 3O_O^{\times} \rightarrow V_{Pu}^{\prime\prime\prime} + V_{Cr}^{\prime\prime\prime} + 3V_O^{\bullet\bullet} + CrPuO_3 \quad (5)$$

$$Pu_{Pu}^{\times} + Cr_{Cr}^{\times} \rightarrow Pu_{Cr}^{\times} + Cr_{Pu}^{\times} \quad (6)$$

The unbound Frenkel energies of Pu, Cr and O are 19.84 eV, 16.64 eV and 9.73 eV (from the O_{II} ion), respectively. As oxygen has the lowest Frenkel energy it should be the most populous defect in a radiation cascade. We compare this to the oxygen Frenkel energy in UO_2, 6.82 eV,[35] which is markedly lower meaning fewer Frenkel pairs should form in $PuCrO_3$. Under equilibrium conditions, the Frenkel defect concentration can be estimated by eqn (7):[38]

$$[O_i^{\prime\prime}] = [V_O^{\bullet\bullet}] = \exp\left(\frac{-E_f}{2kT}\right) \quad (7)$$

where $[O_i^{\prime\prime}]$ is the concentration of interstitials due to Frenkel defects and is equal to the concentration of vacancies $[V_O^{\bullet\bullet}]$, E_f is the Frenkel pair formation energy, 2 is the normalising factor,[39]

Table 4 $PuAlO_3$ defect energies calculated using the Mott–Littleton method

Defect	Defect energy (eV)			
Vacancies				
Pu vacancy	43.83			
Al vacancy	60.29			
O_I vacancy	19.40			
O_{II} vacancy	19.40			
Interstitials				
Site	$\left(\frac{1}{8},\frac{7}{9},\frac{1}{8}\right)$	$\left(\frac{3}{40},\frac{37}{40},0\right)$	$\left(\frac{2}{3},\frac{3}{20},\frac{1}{4}\right)$	$\left(\frac{3}{10},\frac{9}{20},\frac{2}{25}\right)$
Pu interstitial	−21.94	−21.91	−21.18	−21.92
Al interstitial	−43.41	−42.73	−43.51	−43.42
O interstitial	−8.59	−9.43	−9.30	−9.40
Anti-sites				
Pu on Al site	19.00			
Al on Pu site	−12.47			

k is the Boltzmann constant and T is the temperature in Kelvin. At $T = 650$ K, a normal fuel rim temperature, the concentration of Frenkel defects in UO_2 is expected to be 3.65×10^{-27}, and for $PuCrO_3$ it is 1.90×10^{-38}.

The unbound Schottky defect energy for $PuCrO_3$ is 20.20 eV, whilst for UO_2 it is 13.34 eV.[35] Calculating the concentration of defects using the same approach as in eqn (7) but with a normalising factor of 5 for $PuCrO_3$ and 3 for UO_2, the concentration of Schottky defects in $PuCrO_3$ is 4.73×10^{-32}, 3 orders of magnitude higher than that in UO_2 at 3.32×10^{-35}. This is also 6 orders of magnitude higher than the concentration of Frenkel defects in $PuCrO_3$.

Anti-site defects are also important in $PuCrO_3$. When the anti-site energy is low, significant numbers of residual anti-site defects are expected to be retained upon relaxation after a displacement cascade. The anti-site energy for the reaction in eqn (6) is 4.30 eV – the concentration of anti-site defects can be predicted by eqn (8):[36]

$$\left[Cr_{Pu}^{\times}\right] = \left[Pu_{Cr}^{\times}\right] = \exp\left(\frac{-E_f}{2kT}\right) \quad (8)$$

and is calculated to be 2.11×10^{-17}, higher than both the normalised Frenkel and Schottky defect concentrations. The dominant defect should therefore be the antisite defect, which is in agreement with previous work by Cleave *et al.*,[25] which examined the defect behaviour of perovskite-type structures with varying A and B cation radii. The high Frenkel defect energies for $PuCrO_3$ compared to UO_2 will have an impact on the number of defects formed during a radiation cascade, however further work is required to understand the drive for recombination of the defects and the extent to which residual defects are retained.

As with $PuCrO_3$, the vacancy, interstitial and anti-site defect energies were calculated for $PuAlO_3$ using GULP and are given in Table 4. The Frenkel, Schottky and anti-site energies were calculated using reactions analogous to eqn (2)–(6).

The Frenkel energy for Pu is 21.89 eV, for Al, 16.78 eV, and for O, it is the lowest at 9.97 eV. The concentration of Frenkel defects given by eqn (7) is 2.22×10^{-39} at $T = 650$ K. This is 12 orders of magnitude lower than the concentration of Frenkel defects in UO_2 and an order of magnitude lower than in $PuCrO_3$.

The Schottky energy is 18.33 eV, which gives a defect concentration of 3.75×10^{-29}, 6 orders of magnitude higher than in UO_2 and 3 orders of magnitude higher than the Schottky defect concentration in $PuCrO_3$. The anti-site energy is 6.53 eV, higher than that in $PuCrO_3$, indicating that defect recovery in $PuAlO_3$ will leave fewer anti-site defects (and therefore a smaller residual defect population) than in $PuCrO_3$. Calculating the equilibrium concentration using eqn (8) gives an anti-site defect concentration of 4.83×10^{-26}, far smaller than in $PuCrO_3$.

3.4 Solution and partition of minor actinides into $PuCrO_3$

The accommodation of extrinsic, trivalent defects into $PuCrO_3$ was studied. Trivalent cations make up a key proportion of the fission products and oxides that may interact with the $PuCrO_3$ phase, and includes some of the minor actinides (such as Am^{3+}, Cm^{3+} *etc.*) and Fe_2O_3 (potentially present in stainless steel waste-forms and steel cladding). Partition of divalent and tetravalent cations from UO_2 into grey phases was shown to be favourable in previous work by Cooper *et al.*[10]

Solution of trivalent cations from their respective oxides was considered – the results are shown in Fig. 3. A change in the preferred solution mechanism was observed as the extrinsic cation radius increased, with smaller cations preferring to occupy the Cr site, and larger extrinsic cations preferring to occupy the Pu site *via* the following reactions:

$$\frac{1}{2}T_2O_3 + Cr_{Cr}^{\times} \rightarrow T_{Cr}^{\times} + \frac{1}{2}Cr_2O_3 \quad (9)$$

$$\frac{1}{2}T_2O_3 + Pu_{Pu}^{\times} \rightarrow T_{Pu}^{\times} + \frac{1}{2}Pu_2O_3 \quad (10)$$

Larger trivalent cations (T) are predicted to preferentially enter solution into the $PuCrO_3$ phase over remaining in their respective sesquioxide.

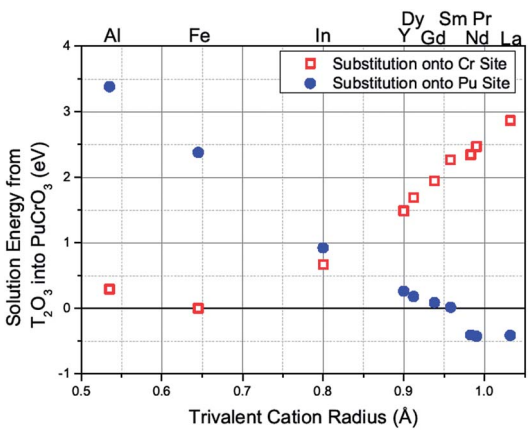

Fig. 3 The solution energy for sesquioxides to enter the $PuCrO_3$ lattice. Trivalent cations are considered to enter onto the Cr site (eqn (11)) and Pu site (eqn (12)) of $PuCrO_3$.

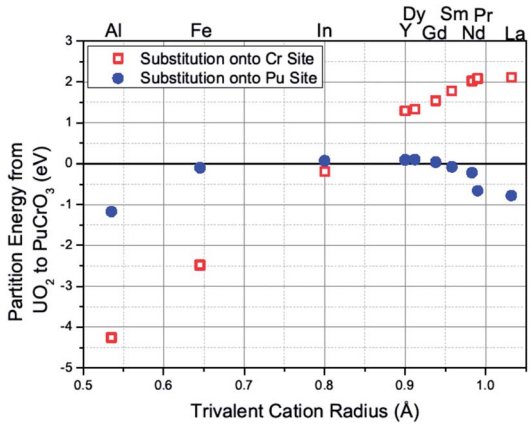

Fig. 4 The partition energy of trivalent cations from UO_2 into $PuCrO_3$. Trivalent cations are considered to enter onto the Cr site (eqn (11)) and Pu site (eqn (12)) of $PuCrO_3$.

The partition energy of these trivalent cations from stoichiometric UO_2 (which allows the formation of $PuCrO_3$) into the $PuCrO_3$ phase is presented in Fig. 4. Trivalent cations are accommodated in stoichiometric UO_2 by the formation of oxygen vacancies to balance the charge of the trivalent cation occupying the uranium site (according to previous work by Middleburgh *et al.*[18]). The partition reactions are:

$$UO_2 + \overline{\frac{1}{2}\{2T'_U : V^{\bullet\bullet}_O\}} + Cr^{\times}_{Cr} \rightarrow \overline{U^{\times}_U + \frac{1}{2}O^{\times}_O} + T^{\times}_{Cr} + \frac{1}{2}Cr_2O_3 \quad (11)$$

$$UO_2 + \overline{\frac{1}{2}\{2T'_U : V^{\bullet\bullet}_O\}} + Pu^{\times}_{Pu} \rightarrow \overline{U^{\times}_U + \frac{1}{2}O^{\times}_O} + T^{\times}_{Pu} + \frac{1}{2}Pu_2O_3 \quad (12)$$

There is a clear preference for small cations, which may be present in the fuel for design purposes (*e.g.* Al^{3+} in ADOPT fuel[4]), and larger trivalent cations, which will include the minor actinides, to segregate into the $PuCrO_3$ structure by one of the two mechanisms. Problem actinides, in waste terms, such as Cm^{3+}, Am^{3+} and Np^{3+}, have ionic radii of 0.97 Å, 0.98 Å and 1.01 Å, respectively, in 6-fold coordination, placing them well within the range of radii for negative partition energy into the secondary phase (*i.e.* they will partition from the UO_2 matrix). The removal and concentration of these species from UO_2 (in which they are normally considered to be soluble) into the $PuCrO_3$ phase may be advantageous when considering fuel reprocessing and disposal. Minor actinides pose a significant challenge in nuclear fuel wastes as their long half-lives ($>10^6$ years) and activity lead to difficulties in waste processing and management which can lead to a considerable increase in the volume of waste. As the fuel designs which contain Cr will separate out the minor actinides, the processing and waste-form production could be considered simpler. The concentration of minor actinides in the residual waste would as a consequence of this separation be significantly reduced.

In terms of HBS formation, the $PuCrO_3$ phase (or a similar phase) may be pivotal in producing clean UO_2 grains, inherent in the restructured rim region.[5] Further, the swelling of the secondary phase in this region may be the cause of the re-crystallisation that is expected to occur on formation of HBS, although further work is required to understand the swelling (and amorphisation) characteristics of the $PuCrO_3$-type perovskite in comparison to the UO_2 in the rim environment.

4 Summary

The effects of doping UO_2 and MOX fuels (in particular Pu containing fuels such as PuO_2–UO_2), with the additives Cr_2O_3 and Al_2O_3, were theoretically investigated by performing structure, defect, solution and thermal conductivity calculations using a range of techniques.

Structure energy calculations using the DFT code, VASP, the empirical potential code, GULP, and the evolutionary structure prediction code, USPEX (used in tandem with GULP), all predicted that when either Cr_2O_3 or Al_2O_3 react with Pu_2O_3, the precipitates $PuCrO_3$ and $PuAlO_3$ would, respectively, form. Furthermore, each method predicts both ABO_3 precipitates to have an orthorhombic (*Pnma*) structure. The result for $PuCrO_3$ is consistent with previous experimental results,[15] but the same authors reported $PuAlO_3$ to have a rhombohedral structure. As the DFT calculations are being carried out at an effective temperature of 0 K, we cannot discount any phase changes that may occur with temperature, rhombohedral or otherwise. Further experimental examination of the $PuAlO_3$ phase (or with a Pu^{3+} analogue such as Nd^{3+}) should be carried out to understand if any phase changes exist. The potential error associated with the empirical calculation predictions may be a result of temperature or the empirical nature of the atomic bonding description.

The thermal conductivities of the $PuCrO_3$ and $PuAlO_3$ precipitates were calculated from non-equilibrium molecular dynamics simulations and compared to the calculated value for stoichiometric UO_2 (using the same fully charged empirical potential set and therefore comparable). The $PuCrO_3$ phase was calculated to have a markedly lower thermal conductivity than UO_2 (similar to that of $LaCrO_3$ (ref. 41)), which will have a distinct knock-on effect upon its supposed formation in the rim region of a standard doped fuel, or dispersed through a MOX fuel pellet. Decreases in thermal conductivity of a pellet will lead to a greater centre line pellet temperature with equivalent rim/clad temperatures. This can lead to microstructural evolution and/or macro-scale effects such as centre line hole formation and a change in fracture behaviour. The effects of radiation damage on the thermal conductivities will be the focus of future work.

The $PuAlO_3$, in both its orthorhombic and rhombohedral structures, showed greater thermal conductivity in comparison to $PuCrO_3$, lower than UO_2 at low temperatures but higher at elevated temperatures. Additions of Al with Cr to doped fuels is therefore likely to have a beneficial impact on the thermal conductivity of the fuel as opposed to solely doping with Cr. The change in thermal conductivity with structure and composition for a number of perovskite structured materials will have

importance in determining the utilization of such materials in a range of components and will be considered in future work.

The radiation tolerances of $PuCrO_3$ and $PuAlO_3$ were investigated by calculating their Schottky, Frenkel and anti-site defect energies. These energies were calculated using GULP. The defect energies in UO_2 were compared with those of the Pu containing precipitates. For both $PuCrO_3$ and $PuAlO_3$, anti-site defects are expected to dominate and thus be the most populous form of defect under thermal equilibrium.

In a radiation cascade (*i.e.* under non-equilibrium conditions), of the three types of Frenkel pairs (two cation and one anion), the oxygen (anion) pair is expected to be the dominant one in both the $PuAlO_3$ and $PuCrO_3$ precipitates. The expected concentration of oxygen Frenkel pair defects in UO_2 is, however, expected to be many orders of magnitude higher than in either precipitate. Further investigation of the Frenkel recombination energy is required to fully compare the radiation tolerance of the precipitates with that of UO_2. However, these results suggest a comparatively low population of defects formed during a radiation cascade (but no stance on recombination and hence residual damage can be solidly given without the kinetic understanding of the system – to be considered in future work).

The solution energies for trivalent cations of varying radii entering solid solution in $PuCrO_3$ from their respective sesquioxides were calculated. The solution energies for substitutions onto both the cation sites showed that smaller cations prefer to occupy the Cr site, whilst larger cations prefer the Pu site. Furthermore, larger cations are predicted to preferentially enter into solid solution in $PuCrO_3$ from their original sesquioxide. When entering into $PuCrO_3$ from stoichiometric UO_2, calculations of the partition energies for these trivalent cations showed that the reaction is favourable for both large and small cations indicating a drive for some trivalent cations to leave the stoichiometric UO_2 lattice. By considering the radius of minor actinides such as Np^{3+} (1.01 Å (ref. 32)), we expect the $PuCrO_3$ phase to act as a getter of trivalent minor actinides.

Acknowledgements

We are grateful to the Australian Nuclear Science and Technology scientific computing group for their support and guidance. This work was supported by the Multi-modal Australian ScienceS Imaging and Visualisation Environment (MASSIVE) (http://www.massive.org.au). Lars Hallstadius, Paul Blair and Radek Jošek from Westinghouse Electric Sweden and Michael Cooper and Robin Grimes from Imperial College London are thanked for their support and discussions on the subject matter.

References

1 R. K. Behera and C. S. Deo, *J. Phys.: Condens. Matter*, 2012, **24**, 215405.
2 J. Wallenius and M. Eriksson, *Nucl. Technol.*, 2005, **152**, 367.
3 C. T. Walker, D. Staicu, M. Sheindlin, D. Papaioannou, W. Goll and F. Sontheimer, *J. Nucl. Mater.*, 2006, **350**, 19.
4 J. Arborelius, K. Backman, L. Hallstadius, M. Limbäck, J. Nilsson, B. Rebensdorff, G. Zhou, K. Kitano, R. Löfström and G. Rönnberg, *J. Nucl. Sci. Technol.*, 2006, **43**(9), 967.
5 C. T. Walker, T. Kameyama, S. Kitajima and M. Kinoshita, *J. Nucl. Mater.*, 1992, **188**, 73.
6 P. Blair, Modelling of fission gas behaviour in High Burnup Nuclear Fuel, PhD thesis, École Polytechnique Fédérale de Lausanne and Paul Scherrer Institute, 2008.
7 J. A. Turnbull, *J. Nucl. Mater.*, 1970, **38**, 203.
8 C. Degueldre, J. Bertsch, G. Kuri and M. Martin, *Energy Environ. Sci.*, 2011, **4**, 1651.
9 K. Une, M. Hirai, K. Nogita, T. Hosokawa, Y. Suzuwa, S. Shimisu and Y. Etoh, *J. Nucl. Mater.*, 2000, **278**, 54.
10 M. W. D. Cooper, D. J. Gregg, Y. Zhang, G. J. Thorogood, G. R. Lumpkin, R. W. Grimes and S. C. Middleburgh, *J. Nucl. Mater.*, 2013, **443**, 236.
11 B. Cox, *J. Nucl. Mater.*, 1990, **172**, 249.
12 P. Burns, R. Ewing and A. Navrotsky, *Science*, 2012, **335**, 1184.
13 B. Ye, Formation and growth of irradiation-induced defect structures in ceria, PhD thesis, University of Illinois at Urbana-Champaign, 2011.
14 W. J. Weber, R. C. Ewing, C. R. A. Catlow, T. Diaz de la Rubia, Hj. Matzke, A. T. Motta, M. Nastasi, E. J. H. Salje, E. R. Vance and S. J. Zinkle, *J. Mater. Res.*, 1998, **13**, 1434.
15 L. E. Russell, D. L. Harrison and N. H. Brett, *J. Nucl. Mater.*, 1960, **2**, 310.
16 M. R. Levy, Crystal Structure and Defect Property Predictions in Ceramic Materials, PhD thesis, University of London, Imperial College London, 2005.
17 P. Dalach, D. E. Ellis and A. van de Walle, *Phys. Rev. B: Condens. Matter Mater. Phys.*, 2012, **85**, 014108.
18 S. C. Middleburgh, D. C. Parfitt, R. W. Grimes, B. Dorado, M. Bertolus, P. R. Blair, L. Hallstadius and K. Backman, *J. Nucl. Mater.*, 2012, **420**, 258.
19 M. W. D. Cooper, S. C. Middleburgh and R. W. Grimes, *J. Nucl. Mater.*, 2013, **438**, 258.
20 A. R. Oganov and C. W. Glass, *J. Chem. Phys.*, 2006, **124**, 244704.
21 J. Gale, *J. Chem. Soc., Faraday Trans.*, 1997, **93**(4), 629.
22 G. Kresse and J. Hafner, *Phys. Rev. B: Condens. Matter Mater. Phys.*, 1993, **47**, 558.
23 R. A. Buckingham, *Philos. Trans. R. Soc., A*, 1938, **168**, 264.
24 R. W. Grimes, D. J. Binks and A. B. Lidiard, *Philos. Mag. A*, 1995, **72**(3), 651.
25 A. R. Cleave, Atomic Scale Simulations for Waste Form Applications, Ph.D. thesis, University of London, Imperial College London, 2006.
26 B. G. Dick and A. W. Overhauser, *Phys. Rev.*, 1958, **112**, 90.
27 G. Kresse and D. Joubert, *Phys. Rev. B: Condens. Matter Mater. Phys.*, 1999, **59**, 1758.
28 B. Dorado and P. Garcia, *Phys. Rev. B: Condens. Matter Mater. Phys.*, 2013, **87**, 195139.
29 N. F. Mott and M. Littleton, *Trans. Faraday Soc.*, 1938, **34**, 485.
30 F. Müller-Plathe, *J. Chem. Phys.*, 1997, **106**, 6082.
31 S. J. Plimpton, *J. Comput. Phys.*, 1995, **117**, 1.
32 R. D. Shannon, *Acta Crystallogr., Sect. A: Cryst. Phys., Diffr., Theor. Gen. Crystallogr.*, 1976, **32**, 751.

33 K. E. Sickafus, L. Minervini, R. W. Grimes, J. A. Valdez, M. Ishimaru, F. Li, K. J. McClellan and T. Hartman, *Science*, 2000, **289**, 748.
34 M. R. Levy, R. W. Grimes and K. E. Sickafus, *Philos. Mag.*, 2004, **164**, 533.
35 R. W. Grimes and C. R. A. Catlow, *Philos. Trans. R. Soc., A*, 1991, **335**, 609.
36 J. A. Ball, S. T. Murphy, R. W. Grimes, D. Bacorisen, R. Smith, B. P. Uberuaga and K. E. Sickafus, *Solid State Sci.*, 2008, **10**, 717.
37 F. A. Kröger and H. J. Vink, *Solid State Phys.*, 1956, **3**, 307.
38 M. R. Levy, K. J. W. Atkinson, O. H. Odili and R. W. Grimes, *Physica B*, 2005, **365**, 147.
39 E. E. Jay, M. J. D. Rushton and R. W. Grimes, *J. Mater. Chem.*, 2012, **22**, 6997.
40 T. Watanabe, S. B. Sinnott, J. S. Tulenko, R. W. Grimes, P. K. Schelling and S. R. Phillpot, *J. Nucl. Mater.*, 2008, **375**, 388.
41 S. P. S. Badwal, *Solid State Ionics*, 2001, **143**, 39.

